

## Visualizing heterogeneous dipole fields by terahertz light coupling in individual nano-junctions

Richard H. J. Kim <sup>1</sup>, Joong M. Park<sup>1</sup>, Samuel Haeuser <sup>1,2</sup>, Chuankun Huang <sup>1,2</sup>, Di Cheng<sup>1,2</sup>, Thomas Koschny<sup>1</sup>, Jinsu Oh <sup>1</sup>, Cameron Kopas <sup>3</sup>, Hilal Cansizoglu<sup>3</sup>, Kameshwar Yadavalli<sup>3</sup>, Josh Mutus<sup>3</sup>, Lin Zhou<sup>1,2</sup>, Liang Luo <sup>1</sup>, Matthew J. Kramer <sup>1</sup> & Jigang Wang <sup>1,2</sup>✉

The challenge underlying superconducting quantum computing is to remove materials bottleneck for highly coherent quantum devices. The nonuniformity and complex structural components in the underlying quantum circuits often lead to local electric field concentration, charge scattering, dissipation and ultimately decoherence. Here we visualize interface dipole heterogeneous distribution of individual Al/AIO<sub>x</sub>/Al junctions employed in transmon qubits by broadband terahertz scanning near-field microscopy that enables the non-destructive and contactless identification of defective boundaries in nano-junctions at an extremely precise nanoscale level. Our THz nano-imaging tool reveals an asymmetry across the junction in electromagnetic wave-junction coupling response that manifests as hot (high intensity) vs cold (low intensity) spots in the spatial electrical field structures and correlates with defected boundaries from the multi-angle deposition processes in Josephson junction fabrication inside qubit devices. The demonstrated local electromagnetic scattering method offers high sensitivity, allowing for reliable device defect detection in the pursuit of improved quantum circuit fabrication for ultimately optimizing coherence times.

<sup>1</sup>Ames National Laboratory, Ames, IA 50011, USA. <sup>2</sup>Department of Physics and Astronomy, Iowa State University, Ames, IA 50011, USA. <sup>3</sup>Rigetti Computing, Berkeley, CA 94710, USA. ✉email: [jgwang@ameslab.gov](mailto:jgwang@ameslab.gov)

A major limitation lies in how to probe deep sub-wavelength electric field distribution under terahertz coupling at individual nano-junctions and correlate them with structural imperfections from interface and boundary, e.g., ubiquitous in Josephson junctions (JJ) structures. The ability to identify heterogeneous electromagnetic field coupling into nano-junctions in quantum circuits is critical to understand and ultimately help guide materials selection and their processing to improve coherence in qubit devices<sup>1</sup>. Materials disorder, structural heterogeneity and interface imperfections are extremely difficult to avoid during complicated lithographic fabrication of the superconducting circuits and junctions. The existence of imperfections have been extensively studied using nano-structural instruments such as scanning and transmission electron microscopy in a destructive manner. However, exactly how the structural heterogeneity affects electromagnetic wave coupling into the quantum circuits as well as electronic field distributions requires non-invasive electronic and photonic nano-THz probes that have not yet been used to map the nano-junctions used in any qubits. Our ability to visualize light-junction coupling at THz-nano scales will enable the determination of salient correlative features and identify previously unobserved error mechanisms, which significantly impact the optimization of fabrication procedures and understanding of decoherence/loss channels of materials and other qubit device components such as JJ structures<sup>2</sup>.

Combining few-cycle THz pulses<sup>3–7</sup> with an atomic force microscope (AFM), time-domain THz scattering-type scanning near-field optical microscopy (THz-sSNOM)<sup>8–21</sup> is an ideal way to capture local conductivity heterogeneity across nano-junctions at nm-THz scales<sup>22–24</sup>. THz is ideal for characterizing Nb and Al superconducting states due to the frequency matching of condensate gaps<sup>25–27</sup> and JJ structure size in transmon qubits. Also, THz is sensitive to the Drude carrier densities<sup>28–30</sup> and phonons<sup>31–33</sup> from the low frequency range of the electromagnetic spectrum, which we anticipate being promising in characterizing local conductivity profiles in individual micro-structures. Applied to the current JJ structures, we envision that such capability well suits in providing useful diagnostics to recent endeavors on the development of quantum materials relevant for superconducting transmon qubit devices. This is partially due to the fact many key components of the qubit circuits exhibit dimensions that match well with THz wavelengths. This condition helps to enhance any near-field effects due to a resonant antenna effect for THz. Furthermore, the metallic conductivity is far less influencing the near-field scattering behavior than local structural defects and nano-gaps.

As illustrated in Fig. 1a, tip-scattered, time-domain THz spectroscopy measures both amplitude ( $s_n$ ) and phase ( $\phi_n$ ) of THz pulses (red arrow) on individual nano-junctions, shown in SEM image (center), which reveal broadband electrical polarizability and local ac charge transport. Although dipole fields in isotropic condensed media exhibit symmetric field and homogeneous electrodynamics, nano-dipoles that are polarized by electromagnetic coupling at junction interfaces are affected by nanoscale inhomogeneities, such as sharp and broken boundaries, as illustrated in Fig. 1b. Such asymmetric boundary conditions, along the upper and lower wings (bottom, Fig. 1a), are spatially correlated with the complicated multi-step deposition procedures used for fabricating Josephson junction structures in transmon qubit fabrication. As illustrated in Fig. 1a, the lower and upper L-shaped aluminum patterns are sequentially deposited on a Si substrate (gray, top left). Here, the AFM tip apex (light blue pyramid) serves as a nanoscale antenna for THz light that encodes the electronic heterogeneity, embedded in the near-field of nano-junction areas, to scattered THz light with distinguishing frequency dependence beyond the conventional topography and

microscopy contrast. Although near-field THz imaging has been prototyped in conventional semiconductors<sup>8,10,11</sup>, semimetals<sup>14</sup> and more recently aluminum resonators on silicon<sup>15</sup>, this method has never been used to study nano-junctions, a critical component in superconduction qubit circuits, such as transmons.

In this letter, we discover asymmetric interface dipole near field distributions and measure THz scattering spectra at sub-20 nm that visualize light coupling into individual junctions. We clearly show that the junction boundaries and interfaces from lithographic procedures strongly affect the light-junction coupling that results in heterogeneous electric field distribution. The nano-electronic and photonic contrasts across junction boundaries manifest as distinguishing nm-THz structures, i.e., distinct variations in the THz-sSNOM amplitude that we denote as hot and cold cusp spatial structures, and a spectral overshoot response where the near-field signal brightens towards the lower end of the THz frequency range. These newly discovered, dipole electric field scattering contrast across nano-junctions are original and distinctly different from topographic steps that exhibit conventional inductive spatial structures and featureless spectral shape. The highly complex responses revealed, together with near-field electromagnetic simulations, clearly show that the room temperature THz-sSNOM results provide foundational knowledge as a basis for understanding any future superconducting state qubit imaging due to the complex nano-photonic structure, electromagnetic coupling and modes involved.

## Results and discussion

Our custom-made THz-sSNOM is based on a tapping-mode atomic force microscope (AFM) excited by ultrashort THz pulses. The AFM metallic tip acts as an antenna that receives far-field THz pulses, amplifies the near-field interaction through an enhancement of the THz field by tip resonances, and finally transmits and scatters the THz near-field to the far field for electro-optical (EO) sampling (Supplementary Note 2). Tip scattering signals  $s(t)$  are extracted by demodulating the back-scattered radiation collected from the tip-sample system at the 2<sup>nd</sup> harmonics of the tip-tapping frequency. To obtain near-field images, the tip was raster scanned over the sample while the THz sampling delay was fixed to a position that gives the maximum amplitude of the THz signal.

Our near-field nano-imaging/spectroscopy experiment was performed on a set of JJ test devices from Rigetti Computing: Al/AlO<sub>x</sub>/Al Josephson junctions fabricated on Si (100) substrates<sup>2</sup> using the nanofabrication procedure for its transmon qubits<sup>34</sup>. The junction comprises two L-shaped aluminum wire leads intersecting at a cross in the middle where a tunneling aluminum-oxide barrier of 1.3 nm separates the two metal layers as illustrated in Fig. 1a (gray pattern, top left) and in Supplementary Note 1. A scanning electron microscopy (SEM) image in Fig. 1a (center), shows the junction area of ~1-to-2 micrometers across in size that is analyzed in our study. The JJ is defined by the region where an upper lead overlaps a lower lead separated by an insulating oxide layer shown at the center of the SEM image in Fig. 1a. The junction area is amplified (lower) to highlight the boundaries across the lower and upper wings. The JJs are fabricated in micro- to nano-scale area dimensions to reduce lossy channels from forming on the device interfaces and surfaces. Some degree of structural asymmetry and discontinuity are expected due to the geometry of double-angle shadow evaporation techniques commonly used to fabricate JJs. The noninvasive THz nanoscopy technique allows us to probe the local electric field distributions in these areas and correlate them with structural features, such as dislocations, vacancies, and grain boundaries. The scattering spectra at THz-nano scales are critical to

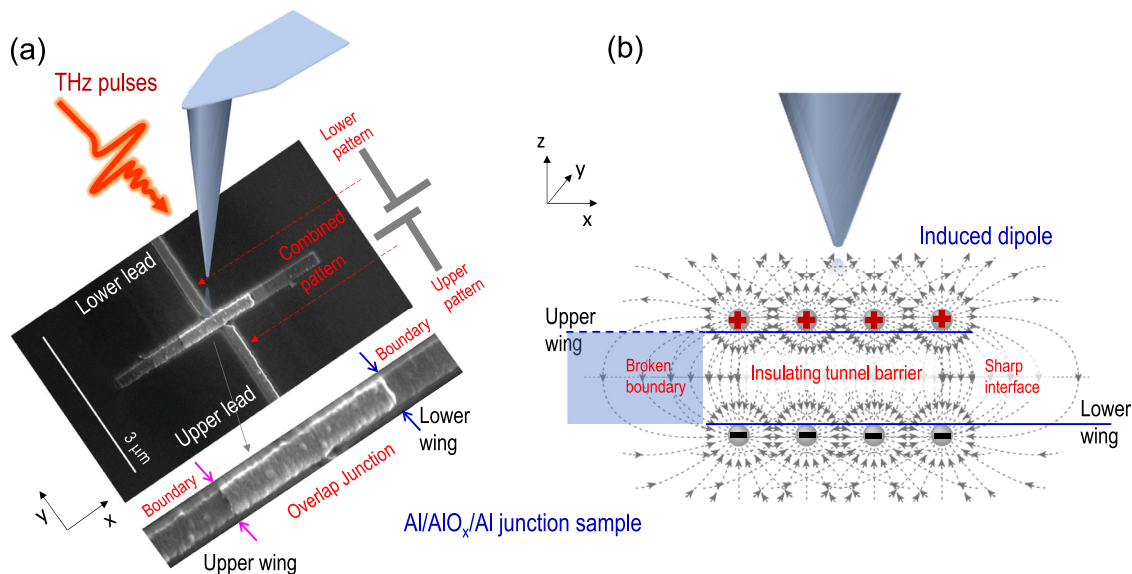


**Fig. 1 THz nano-imaging of Al/AIO<sub>x</sub>/Al junction nano-dipole fields.** **a** Schematic of the THz-sSNOM imaging method showing an incoming THz pulse to an AFM tip and an aluminum Josephson junction below it displayed as an SEM image. An enlarged image of the junction area is shown at the bottom. **b** Illustration of the formation of dipole fields at one instant of time as the incoming THz electric field induces free carriers in both sides of the metal lead to polarize the structure with opposite charges as in a capacitor.

identifying unfavorable electric scattering and dissipation mechanisms that limit quality factors in individual nano-junctions. Once our THz pulse impinges on the sample in our near-field measurement, the highly enhanced electric field from the tip induces a series of oscillating dipole field patterns reminiscent to an ac-driven capacitor as illustrated in Fig. 1b, as the tip is scanned across the surface. Opposite charges reside on the two different metallic layers at a given instant of time. Stray fields along the edges of the junction, where only the upper or the lower lead is found, are very sensitive to the local dielectric environment and can deviate from the uniform fields near the center; thus correlating nano-scale structural and electronic heterogeneous behavior at THz frequencies.

To this end, a direct visualization of the THz near-field electrodynamics through light-junction coupling demonstrates a dramatic asymmetric contrast across the junction area. Figure 2a presents a typical scan on a Josephson junction showing a highly reflecting tip-scattered near-field amplitude from the lower aluminum junction wing and a darker contrast along the upper wing and lead structure. Figure 2b shows an identical scan of the region after rotating the sample 180 degrees in the *x-y* plane. This confirms that the striking uneven brightness of the electric field scattering amplitude between the junction wing and lead wires is independent on the direction of, and thereby, direct interaction with, the propagating field of the incident beam of THz light. It is rather related to the near-field coupling and nanoscale intrinsic junction properties. An AFM map taken simultaneously with our THz-sSNOM measurement, displayed in Fig. 2c, further indicates that the asymmetric near-field signal across the nano-junction wings does not correlate with the topographic features of the junctions. The lower (upper) metal wing layer shows the brightest (darkest) THz scattered amplitude whereas the highest overlapping region at the center exhibit a moderate near-field intensity. Additional THz-sSNOM scans acquired on two other junction devices, shown in Fig. 2f, g reveal the same asymmetric near field distribution of the scattered THz electric field with the nano-dipole field mostly concentrated toward the lower wing adjacent to the center junction. This conclusively demonstrates

the discovered asymmetric nano-dipole field contrast is universal to the Josephson junctions fabricated using double-angle deposition techniques.

For a quantitative analysis of the THz near-field amplitude images, Fig. 3a, b plot line scans running along the middle of the junction and across the single wire lower lead (inset, Fig. 3b) designed to connect the junction to the communication lines. The highly asymmetric feature in the nano-electronic contrast is easily discerned in the line profile of the THz near-field amplitude (thick red line) when compared with the height profile (thin gray line) measured simultaneously as shown in Fig. 3a. We observed two distinct different contrasts. First, a topographic crosstalk leads a conventional THz near-field contrast that edge effects occur at sharp material boundaries near to the silicon substrate<sup>35,36</sup>. This effect is most obvious at the edges of the wire leads as shown in Fig. 3b. There is a sharp inductive spatial variation of the near-field signal as the AFM tip approaches the aluminum-substrate interface. At this lower edge, the AFM tip increases the total area of interaction with the sample, and thus increases the total near field signals. Consequently, the signal suddenly drops when the tip approaches the top of the edge and couples weakly with the sample structure. Second, the nano-dipole electric field scattering contrast sets in across nano-junctions as elaborated in detail below.

A drastically different contrast appears near the junction interface, in comparison with the expected topographic near-field contrast around the low lead edges of the device (Fig. 3b). As shown in Fig. 3a (thick red line), the THz scattered amplitude increases as the tip moves toward the midpoint from both sides; however, the side associated with the upper aluminum wing displays a sudden drop in the amplitude as it meets the junction. Immediately next to the local maximum of the scattered signal of this upper lead, which we call the cold cusp, a deep trench is visible that most likely indicates a discontinuity or a break in the metallic structure. The deep trench is absent in the lower wing of the junction interface. At the very top of the junction, the near-field amplitude returns to the signal level that is similar to silicon. Most intriguingly, the THz amplitude reaches its maximum and

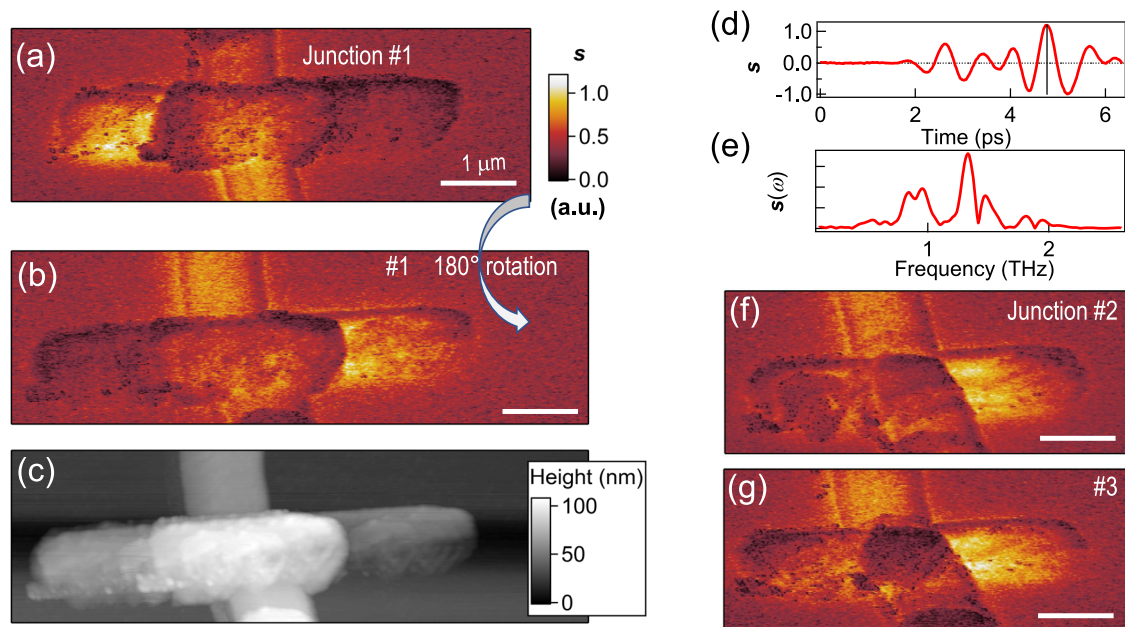


**Fig. 2 Representative THz near-field images of nano-dipole fields across Josephson junction structures.** **a** Spatial mapping of the THz near-field scattering amplitude  $s$  measured on a junction area in a 2D false color plot. **b** THz near-field image of the same area in **a** after rotating the sample 180 degrees in the sample plane. **c** A simultaneously acquired AFM topography image of the same region in **b**. **d, e** A typical time-resolved THz near-field waveform measured on the sample and its Fourier transformed spectrum. **f, g** THz near-field contrast images of two additional Josephson junctions.

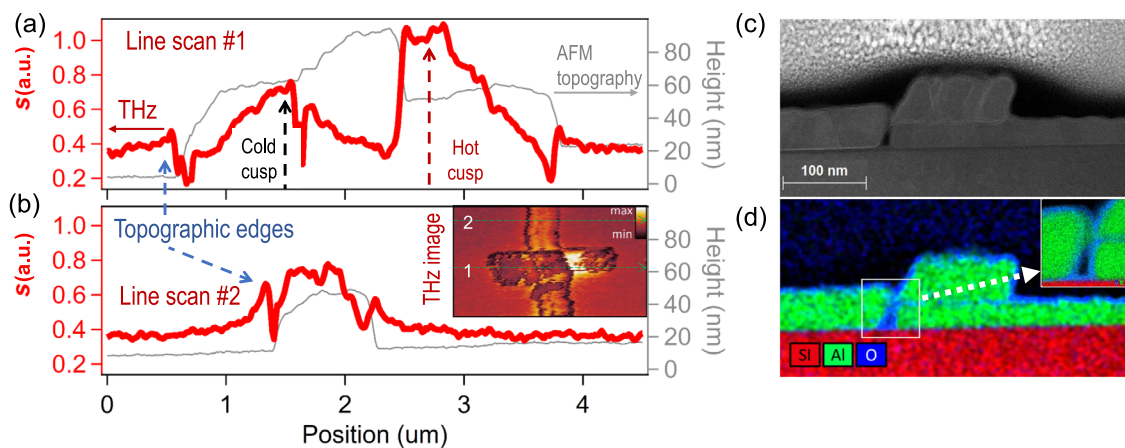


**Fig. 3 Nano-electronic and photonic vs. topographic profiles that show lithographic fingerprints of nano-gaps in junction fabrication.** Line cuts of the near-field amplitude (red) and topography (gray) **(a)** along the direction from the upper wing to the lower wing across the center of the junction and **(b)** across the lower wire lead. **c** Cross-section high-angle annular dark-field STEM image of a Josephson junction and the corresponding EDS elemental mapping **(d)** that shows the disconnection of the upper wing to the center piece of the junction.

forms a high plateau near the lower lead which we designate as the hot cusp. Such spatial evolution of the hot and cold cusp features consistent with different local dielectric environment and nano-dipole electric fields. The THz signal shows a clearly different behavior even in areas where the height variation is almost identical, i.e., there exists a new image contrast from electronic/structural heterogeneity beyond the trivial topographical cross-talk. To correlate the local electronic response with structural one, a cross-section image was obtained along the center of the nano-junction by employing scanning transmission electron microscopy (STEM) and energy dispersive X-ray spectroscopy (EDS) elemental mapping, as shown in Fig. 3c, d, respectively. We can see a clear separation along the upper lead that corresponds to the sharp near-field signal drop in the cold cusp region. The EDS elemental mapping confirms the gap is partially filled with oxides and forms on one side of the nano-junction due to the possible

shadowing from the step of the lower lead's edges during the deposition process of the upper leads. These distinguishable hot and cold near-field intensity differences between the lower and upper aluminum layers demonstrates that the THz near-field scattering amplitude provides valuable insights on possible spatial variations in the continuity between the two metallic layers. The presence of an isolated metallic island adjacent to a Josephson junction can act as an independent Cooper pair box. Such configuration can introduce additional charge noise during qubit operations. Note that the THz-sSNOM images are obtained in a nondestructive way while other mappings are obtained by destructively cutting the nano-junctions.

We further conducted THz nano-spectroscopy on different positions of the junction to examine the electronic scattering and dissipation channels implied in the observed heterogeneous electrodynamics. By choosing four positions, as indicated in the inset



of Fig. 4b, we obtain the time dependent electric field waveform of the THz scattering response  $s$ , shown in Fig. 2d. A fast Fourier transform was performed on the resulting time traces to yield a near-field amplitude  $|s(\omega)|$ , as shown in Fig. 2e, and the phase  $\arg\{s(\omega)\}$  spectra. The resulting relative scattering amplitudes and phases are plotted in Fig. 4a, b, respectively, with one spectrum recorded from the silicon substrate serving as a reference. The spectra include the normal interruptions at 1.1 THz and 1.4 THz which arise from the dipole resonance of the AFM tip and cantilever assembly matching the THz wavelength (Supplementary Note 4). Additionally, the phase spectra include a slight shift from the insulating silicon substrate as is expected for the metallic components that form these junctions. Interestingly, we find that brighter hot cusp regions are more than twice the magnitude in

the near-field amplitude than that from darker cold cusp portions of the junction. We also find the brighter hot cusp regions exhibit a spectral slope curving upwards toward lower frequencies. As the entire metallic structure that connects to the small Josephson junction area amounts to the area of several hundreds of micrometers squared, it is likely that the light couples more efficiently with longer wavelengths of the impinging THz beam. Thus, the near-field scattered amplitude will be enhanced in the lower part of the THz frequency spectrum. As SEM images identified that grain sizes are smaller and the film being more granular for the lower layer aluminum, the higher signal contrast here determined from our THz sSNOM measurement suggests that the actual conductivity is governed by other factors, such as the sequential order of the substrate etching process and to the lithography steps used in the Josephson junction fabrication, while the granularity of the aluminum films is less of a contributing factor to the electric scattering.

Finally, in order to understand better how the near-field effects contribute in which way to the observed signal during the measurement, we simulate a simplified model for the individual contributions of tip/cantilever modes, resonant nanostructure modes, and tip near-field effects numerically in COMSOL (Supplementary Note 3). Because of the vastly different length-scales involved, it is numerically not feasible to simply model the whole SNOM/nanostructure/substrate geometry in a single consistent finite elements simulation. This would require unrealistic numbers of mesh elements and memory: Elements size of few nanometers to capture the strongly varying resonant near-fields of the tip (20 nm curvature radius) and the near field of the defects in the JJ structure (tens of nanometer length scale) over a simulation domain of the order of several millimeters to correctly capture the eigenmodes of the SNOM setup (~1 mm tip/cantilever assembly) and the geometry of the THz beam reflection of the substrate/sample. We, therefore, radically approximate by segregating the different length-scales (tip/cantilever assembly eigenmodes, JJ-feeder eigenmodes, and near-field tip interaction) into separate, much simplified models to illustrate their individual contributions while preserving the qualitative physical scattering mechanisms. The JJ is modeled based on the schematics shown in Fig. 5a, b,

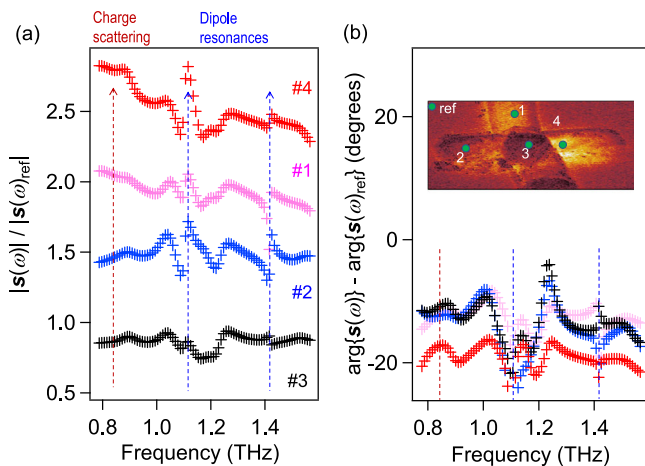


**Fig. 4 Heterogeneous THz electrodynamics in a single nano-junction.** **a** Near-field spectral amplitude  $|s(\omega)|$  and **(b)** phase  $\arg\{s(\omega)\}$  acquired by a Fourier transform of the time-domain signal as shown for example in Fig. 2d. The results are normalized by another Fourier-transformed trace taken at the silicon substrate. Spectrums are taken at positions indicated in the inset of **b**. Inset is identical to the THz image shown in Fig. 2g.

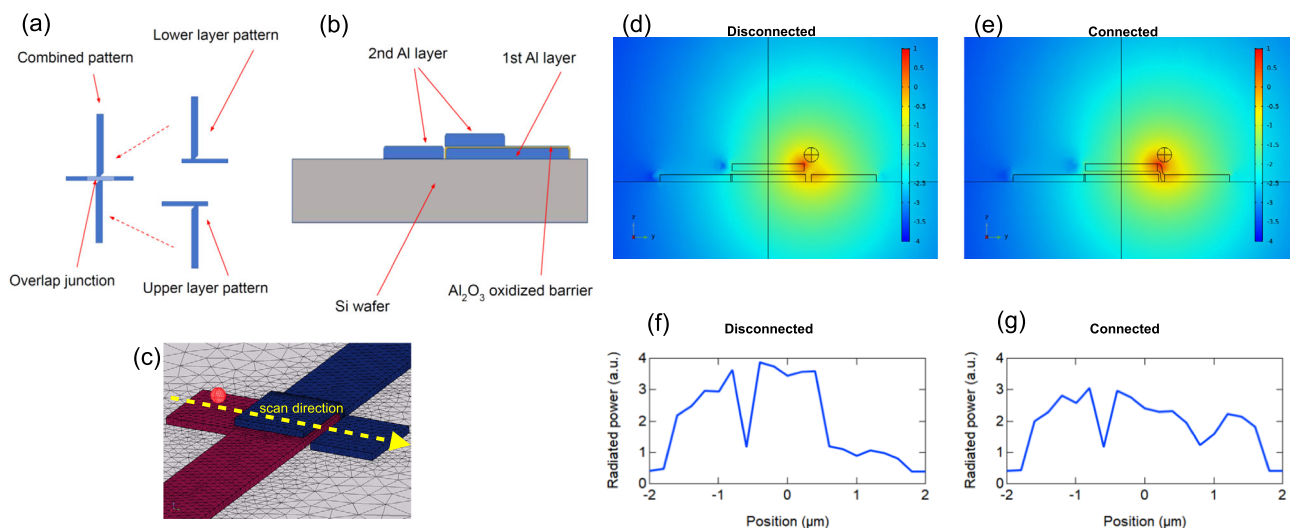


**Fig. 5 Simulations of the THz near-field asymmetry across a Josephson junction.** **a** Schematic diagram showing the Josephson junction composed of a double-L structure and **(b)** its cross-sectional view. **c** Simulation geometry of the Josephson junction and the spherical dipole source. Simulation results showing the scattered field distribution around the dipole source and the junction for the disjointed case **(d)** and the contiguous case **(e)**. The abstract spherical dipole source above the sample drives the Josephson junction structure through near-field coupling. Far-field scattered power for different locations of the dipole source across the Josephson junction shows **(f)** the asymmetric response when the break is present in the upper lead whereas **(g)** a relatively homogeneous signal is shown for the fully connected leads.

with the actual simulation conducted using the geometry presented in Fig. 5c. By comparing the contiguous junction with the experimental structure featuring a break in the top layer of the junction (the existence of which is independently proven by TEM), we demonstrate that we indeed would expect to see a significant change in the SNOM signal for a pristine vs. defective JJ element as is demonstrated in the simulation results shown in Fig. 5d–g. We observe a clear difference in the scattered fields depending on whether the upper aluminum wire is connected toward the winged part of the structure or is disconnected from it. We let the point dipole traverse the upper contour of the junction and observe how the scattered field changes at different positions. The scattered fields are shown to be weaker when the tip lands on the aluminum island but maintains its strength that is at the same level as the opposite part of the wing when the upper wire fully connected. We conclude that the strong asymmetric scattering results of the disconnected junction agrees well with our near-field experiment proving that the difference and pronounced right-left asymmetry is indeed expected for the broken JJ in comparison to a pristine continuous JJ. We note that finding out the exact magnitude of near-field signals poses a complicated, multi-scale simulation problem and warrants for further investigations. Our current simulations based on physics-guided near-field scattering model already demonstrate the most salient image contrast, i.e., an asymmetry in the scattered field is clear in both our simulations and experiments.

In conclusion, we directly image THz light coupling into an individual nano-junction and discover deeply sub-wavelength heterogeneous near-field electrodynamics at nm scales. The demonstrate method surpasses the limitations of conventional microscopy tools, which lack the capability to measure simultaneously at both nanometer and terahertz scales. These scales are particularly important when dealing with frequency-dependent electromagnetic scattering in nano-junctions. The near-field THz interrogation of a frequency-dependent effective polarizability provides a way of noninvasively identifying the junction interfaces and structural boundaries. The information obtained on the electric field distribution is highly complementary to destructive cross sectional characterization using STEM. Thus, the non-destructive time-domain THz scattering-type scanning near-field optical microscopy system shows promise in detecting possible variations in the thin-film fabrication processes hidden to surface imaging techniques. As low-temperature characterization of complete qubit chips is costly and cannot be done in a high-throughput fashion, rapid room temperature screenings of individual qubit components provide an important guidance on structure and materials screening in order to build successful qubit devices. Since the structural discontinuity inevitably results from the complicated lithography and evaporation technique in the fabrication of the JJs and qubit circuits, the THz nano-imaging technique is useful to identify defective structures during the fabrication processes to facilitate the screening of good vs bad qubit chips. The THz nanoscopy and amplitude-phase analysis are being further extended to cryogenic temperatures for capturing Cooper pair tunneling and circulation through Josephson junction devices<sup>21</sup>. We anticipate that near-field images from the THz-SNOM measurements will reveal the electromagnetic field distributions around the structure which relates to the local charge and current distributions from the tunneling Cooper pairs through the junction.

## Methods

**Sample preparation.** The Al/AlO<sub>x</sub>/Al Josephson Junction test structures are fabricated on high-resistivity Si (100) substrates ( $\rho \geq 10000 \Omega \cdot \text{cm}$ ). The JJ structure is defined by patterning an MMA PMMA resist bilayer using electron beam lithography. Following definition of the pattern, the structure is deposited by double-

angle electron beam evaporation of two Al layers with an in-situ controlled oxidation step in between. Excess material and resist are removed by a solvent lift-off process. One method to integrate a similar JJ process into qubit fabrication can be found in ref. <sup>2</sup>.

**THz-sSNOM experimental setup.** THz nano-imaging and nano-spectroscopy measurements are carried on using our custom-made compact THz-sSNOM set-up built on a tapping-mode atomic force microscope (Attocube systems AG) with a metallic tip (Rocky Mountain Nanotechnology, LLC). The tip acts as an antenna which receives and scatters far-field THz radiation while amplifying the near-field interaction with the sample surface through a resonant enhancement of the THz field. The THz-sSNOM setup is driven by a Yb fiber laser operating at a repetition rate of 1 MHz with a pulse width of 147 fs and a center wavelength at 1038 nm. THz pulses are generated by optical rectification in a 540- $\mu\text{m}$ -thick THz generation crystal with a pulse energy of  $>2 \mu\text{J}$ . THz electric fields are detected via electro-optic sampling. Scattered near-field signals  $s_n$  ( $n = 1, 2$ , and 3) are extracted using a lock-in amplifier by demodulating the backscattered radiation collected from the tip-sample system at  $n$ th harmonics of the tip-tapping frequency. All the data presented is from demodulated, 2<sup>nd</sup> order near-field signals  $s_2$ . To obtain near-field images, the tip was raster scanned over the sample while the THz sampling delay was fixed to a position that gives the maximum amplitude of the THz signal. Nano-spectroscopy is achieved by scanning the THz sampling delay to directly trace out the oscillating THz electric field waveforms in the time domain by photoconductive antennas while the tip positions at a fixed location on the sample.

**STEM and EDS measurements.** TEM samples were prepared using a Helios (Thermo Fisher Scientific Ltd.) dual beam focused ion beam system. The TEM samples were thinned to electron beam transparency by a Ga<sup>+</sup> ion beam from 30 to 2 kV. The TEM samples were then investigated using an aberration-corrected TEM (Titan Cube, Thermo Fisher Scientific Ltd.) at 200 kV. Dark-field STEM imaging was conducted using a high angle annular dark-field detector with a convergent semi-angle and a collection semi-angle of 18 mrad and 74–200 mrad, respectively. EDS elemental mapping was carried out with a probe current of 150 nA.

## Data availability

The data that support the plots within this paper and other findings of this study are available from the corresponding author upon reasonable request.

Received: 15 July 2022; Accepted: 2 June 2023;

Published online: 22 June 2023

## References

- Preskill, J. et al. Quantum computing in the NISQ era and beyond. *Quant. Austria* **2**, 79 (2018).
- Nersisyan, A. et al. Manufacturing low dissipation superconducting quantum processors. 2019 *IEEE International Electron Devices Meeting (IEDM)* pp. 31.1.1–31.1.4 (San Francisco, CA, USA, 2019).
- Yang, X. et al. Terahertz-light quantum tuning of a metastable emergent phase hidden by superconductivity. *Nat. Mater.* **17**, 586–591 (2018).
- Yang, X. et al. Lightwave-driven gapless superconductivity and forbidden quantum beats by terahertz symmetry breaking. *Nat. Photonics* **13**, 707–713 (2019).
- Liu, Z. et al. Ultrafast control of excitonic rashba fine structure by phonon coherence in the metal halide perovskite CH<sub>3</sub> NH<sub>3</sub> PbI<sub>3</sub>. *Phys. Rev. Lett.* **124**, 157401 (2020).
- Yang, X. et al. Nonequilibrium pair breaking in Ba(Fe<sub>1-x</sub>Co<sub>x</sub>)<sub>2</sub>As<sub>2</sub> superconductors: evidence for formation of a photoinduced excitonic state. *Phys. Rev. Lett.* **121**, 267001 (2018).
- Luo, L. et al. Broadband terahertz generation from metamaterials. *Nat. Commun.* **5**, 3055 (2014).
- von Ribbeck, H.-G. et al. Spectroscopic THz near-field microscope. *Opt. Express* **16**, 3430–3438 (2008).
- Moon, K. et al. Subsurface nanoimaging by broadband terahertz pulse near-field microscopy. *Nano Lett.* **15**, 549–552 (2014).
- Aghamiri, N. A. et al. Hyperspectral time-domain terahertz nano-imaging. *Opt. Express* **27**, 24231–24242 (2019).
- Liewald, C. et al. All-electronic terahertz nanoscopy. *Optica* **5**, 159–163 (2018).
- Chen, H.-T., Kersting, R. & Cho, G. C. Terahertz imaging with nanometer resolution. *Appl. Phys. Lett.* **83**, 3009–3011 (2003).
- Zhang, J. et al. Terahertz nanoimaging of graphene. *ACS Photonics* **5**, 2645–2651 (2018).
- Kim, R. H. J. et al. Terahertz nano-imaging of electronic strip heterogeneity in a Dirac semimetal. *ACS Photonics* **8**, 1873–1880 (2021).

15. Guo, X. et al. Near-field terahertz nanoscopy of coplanar microwave resonators. *Appl. Phys. Lett.* **119**, 091101 (2021).
16. Stinson, H. T. et al. Imaging the nanoscale phase separation in vanadium dioxide thin films at terahertz frequencies. *Nat. Commun.* **9**, 3604 (2018).
17. Klarskov, P., Kim, H., Colvin, V. L. & Mittleman, D. M. Nanoscale laser terahertz emission microscopy. *ACS Photonics* **4**, 2676–2680 (2017).
18. Pizzuto, A. et al. Anomalous contrast in broadband THz near-field imaging of gold microstructures. *Opt. Express* **29**, 15190–15198 (2021).
19. Wang, K., Mittleman, D. M., van der Valk, N. C. J. & Planken, P. C. M. Antenna effects in terahertz apertureless near-field optical microscopy. *Appl. Phys. Lett.* **85**, 2715 (2004).
20. Kim, R. H. J. et al. Terahertz nanoimaging of perovskite solar cell materials. *ACS Photonics* **9**, 3550–3556 (2022).
21. Kim, R. H. J., Park, J.-M., Haeuser, S. J., Luo, L. & Wang, J. A sub-2 Kelvin cryogenic magneto-terahertz scattering-type scanning near-field optical microscope (cm-THz-sSNOM). *Rev. Sci. Instrum.* **94**, 043702 (2023).
22. Cocker, T. L., Jelic, V., Hillenbrand, R. & Hegmann, F. A. Nanoscale terahertz scanning probe microscopy. *Nat. Photonics* **15**, 558–569 (2021).
23. Kimura, K. et al. Terahertz-field-driven scanning tunneling luminescence spectroscopy. *ACS Photonics* **8**, 982–987 (2021).
24. Plankl, M. et al. Subcycle contact-free nanoscopy of ultrafast interlayer transport in atomically thin heterostructures. *Nat. Photonics* **15**, 593–600 (2021).
25. Luo, L. et al. Quantum coherence tomography of lightwave-controlled superconductivity. *Nat. Phys.* **19**, 201 (2023).
26. Vaswani, C. et al. Light quantum control of persisting higgs modes in iron-based superconductors. *Nat. Commun.* **12**, 258 (2021).
27. Xu, Y. et al. Ultrafast nonthermal terahertz electrodynamics and possible quantum energy transfer in the  $N_s$  Sn superconductor. *Phys. Rev. B* **99**, 094504 (2019).
28. Song, B. Q. et al. Ultrafast martensitic phase transition driven by intense terahertz pulses. *Ultrafast Sci.* **3**, 0007 (2023).
29. Luo, L. et al. Ultrafast bipolar conductivity driven by intense single-cycle terahertz pulses in a topological insulator  $\text{Bi}_2\text{Se}_3$ . *J. Optics* **23**, 104003 (2023).
30. Luo, L., Chatzakos, I., Patz, A. & Wang, J. Ultrafast terahertz probes of interacting dark excitons in chirality-specific semiconducting single-walled carbon nanotubes. *Phys. Rev. Lett.* **114**, 107402 (2015).
31. Luo, L. et al. A light-induced phononic symmetry switch and giant dissipationless topological photocurrent in  $\text{ZrTe}_5$ . *Nat. Mater.* **20**, 329 (2021).
32. Vaswani, C. et al. Light-driven Raman coherence as a nonthermal route to ultrafast topology switching in a Dirac semimetal. *Phys. Rev. X* **10**, 021013 (2020).
33. Luo, L. et al. Ultrafast manipulation of topologically enhanced surface transport driven by mid-infrared and terahertz pulses in  $\text{Bi}_2\text{Se}_3$ . *Nat. Commun.* **10**, 607 (2019).
34. Lecocq, F. et al. Junction fabrication by shadow evaporation without a suspended bridge. *Nanotechnology* **22**, 315302 (2011).
35. Taubner, T., Hillenbrand, R. & Keilmann, F. Performance of visible and mid-infrared scattering-type near-field optical microscopes. *J. Microsc.* **210**, 311–314 (2003).
36. Babicheva, V. E., Gamage, S., Stockman, M. I. & Abate, Y. Near-field edge fringes at sharp material boundaries. *Opt. Express* **25**, 23935 (2017).

## Acknowledgements

This work was supported by the U.S. Department of Energy, Office of Science, National Quantum Information Science Research Centers, Superconducting Quantum Materials

and Systems Center (SQMS) under the contract No. DE-AC02-07CH11359 (THz-sSNOM measurements, Josephson junction fabrication and characterizations, STEM characterizations, cryogenic instrumentation upgrade), and by the Ames Laboratory, the US Department of Energy, Office of Science, Basic Energy Sciences, Materials Science and Engineering Division under contract No. DEAC02-07CH11358 (Basic scanning probe microscopy characterizations and THz microscopy modelling). Upgrade of THz-sSNOM for improved cryogenic operation was supported by the US Department of Energy, Office of Science, National Quantum Information Science Research Centers, Superconducting Quantum Materials and Systems Center (SQMS) under the contract No. DE-AC02-07CH11359. Initial design and commission of THz-sSNOM instrument was developed by the support from W. M. Keck Foundation.

## Author contributions

R.H.J.K., J.M.P. and S.H. performed the THz imaging measurements with J.W.'s supervision. J.O., L.Z., and M.K., performed STEM measurements and analysis. T.K. developed near-field scattering model and performed simulations. C.K., H.C., K.Y., and J.M., fabricated nano-junctions and performed basic transport characterizations. J.W. and R.H.J.K. analyze the data with the help of C.H., D.C., L.L. The paper is written by J.W., R.H.J.K. and T.K. with discussions from all authors. J.W. envisioned and coordinated the project.

## Competing interests

C.K., H.C., K.Y., and J.M. have been, or may in the future be participants in incentive stock plans at Rigetti Co Inc. The other authors declare that they have no competing interests.

## Additional information

**Supplementary information** The online version contains supplementary material available at <https://doi.org/10.1038/s42005-023-01259-0>.

**Correspondence** and requests for materials should be addressed to Jigang Wang.

**Peer review information** *Communications Physics* thanks the anonymous reviewers for their contribution to the peer review of this work.

**Reprints and permission information** is available at <http://www.nature.com/reprints>

**Publisher's note** Springer Nature remains neutral with regard to jurisdictional claims in published maps and institutional affiliations.



**Open Access** This article is licensed under a Creative Commons Attribution 4.0 International License, which permits use, sharing, adaptation, distribution and reproduction in any medium or format, as long as you give appropriate credit to the original author(s) and the source, provide a link to the Creative Commons license, and indicate if changes were made. The images or other third party material in this article are included in the article's Creative Commons license, unless indicated otherwise in a credit line to the material. If material is not included in the article's Creative Commons license and your intended use is not permitted by statutory regulation or exceeds the permitted use, you will need to obtain permission directly from the copyright holder. To view a copy of this license, visit <http://creativecommons.org/licenses/by/4.0/>.

© The Author(s) 2023